ACS Catalysis

Research Article

pubs.acs.org/acscatalysis

Embedding Pt Nanocrystals in N-Doped Porous Carbon/Carbon Nanotubes toward Highly Stable Electrocatalysts for the Oxygen Reduction Reaction

Lin Guo,[†,‡] Wen-Jie Jiang,[†] Yun Zhang,[†,‡] Jin-Song Hu,*[,†] Zi-Dong Wei,*[,‡] and Li-Jun Wan[†]

[†]Beijing National Laboratory for Molecular Sciences, Key Laboratory of Molecular Nanostructure and Nanotechnology, Institute of Chemistry, Chinese Academy of Science, 2 North First Street, Zhongguancun, Beijing 100190, China

[‡]State Key Laboratory of Power Transmission Equipment & System Security and New Technology, College of Chemistry and Chemical Engineering, Chongqing University, Chongqing 400044, China

S *Supporting Information*

ABSTRACT: The development of highly stable and efficient catalysts for sluggish cathode oxygen reduction reaction (ORR) is extremely important for the long-term operation and the commercialization of proton exchange membrane fuel cells (PEMFCs) but still challenging. We present herein a facile strategy to efficiently embed Pt nanocrystals into N-doped porous carbon/carbon nanotubes (Pt@CN*x*/CNT). The N-doped porous carbon shells not only effectively prevented Pt nanocrystals from detachment, dissolution, migration, and aggregation during accelerated durability tests or heat-treatment at 900 °C, but also allowed the access of electrolyte to the Pt surface and preserved the good electron transfer of CNT by avoiding the structural damage of carbon nanotubes (CNTs). The interaction between the embedded Pt nanocrystals and the encapsulating CN*x* layer was found in Pt@CN*x*/CNT, which markedly affected the electronic structure of Pt nanocrystals and contributed to the improvement on the catalytic activity and stability of Pt@CN*x*/CNT. As a result, the Pt@CN*x*/CNT catalyst exhibited an excellent thermal stability, durability, and sufficient catalytic activity for ORR. The demonstrated strategy could be easily extended to produce a wide range of other electrocatalysts with even better activity and extraordinary stability.

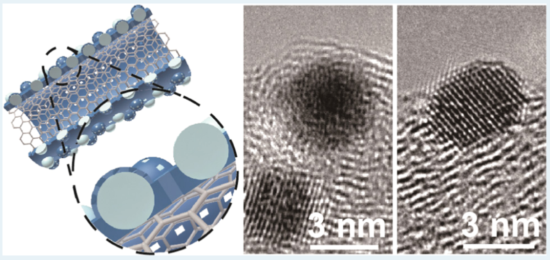

KEYWORDS: *PEMFCs, platinum, N-doped carbon, high durability nanostructures*

1. INTRODUCTION

As worldwide demands for exploiting a sustainable energy supply and reducing environmental pollution continue to increase, proton exchange membrane fuel cells (PEMFCs) have attracted considerable attention as one of the most promising energy conversion devices for automotive and stationary applications because of their high energy conversion efficiency, low emissions, and renewable fuels. For PEMFCs to quickly reach commercial implementation, developing a promising catalyst for the oxygen reduction reaction (ORR) is of great importance.[1,2] At present, Pt nanoparticles (NPs) on a carbon support (Pt/C) is still considered as one of the most efficient catalysts for ORR. Supporting Pt NPs on carbon increases the electrochemical activity and utilization of Pt and, thus, effectively decreases the overall cost of PEMFCs. However, the stability of Pt/C for ORR cannot meet the requirement for the long-term operation of PEMFCs owing to the rapid loss of electrochemical surface area (ECSA) and the performance.[3−5]

Under the corrosive operating conditions in strong acidic media (pH < 1) and highly positive potentials even up to 1.5 V, etc., carbon supports are easily oxidized, which results in the detachment of Pt NPs from the carbon support and, thus, the performance loss.[6−9] Meanwhile, the Pt dissolution, eventually followed by particle growth due to Ostwald ripening, would take place.[3,10,11] Furthermore, the migration and agglomeration of Pt NPs on the carbon surface cannot be effectively suppressed by the weak interaction between the carbon support and Pt NPs.[11] Therefore, enormous studies have attempted to solve these issues, including improving the carbon support with other species, such as a polymer, organic group, or metal oxide;[12−14] designing new Pt nanostructures, such as mesoporous particles, nanowires, and nanotubes;[15−20] forming multimetallic Pt alloys with other transition metals, such as Y, Ni, Co, and Ga;[21−24] developing a more corrosion-resistant support, such as $Ta_{0.3}Ti_{0.7}O_2$ and TiO_2;[25,26] and enhancing the interaction between Pt and the supports by employing a modified support, such as SH−CNTs, $Ti_{0.7}Mo_{0.3}O_2$, and $Co_6Mo_6C_2/C$.[27−29] The resulting catalysts exhibit improved corrosion resistance and reasonable activity for ORR; however, the improved stability of such catalysts usually comes at the cost of a significant increase in the size of the Pt NPs or a decrease in the catalyst conductivity, which does not favor the

Received: January 21, 2015
Revised: March 26, 2015
Published: March 26, 2015

DOI: 10.1021/acscatal.5b00117
ACS Catal. 2015, 5, 2903−2909

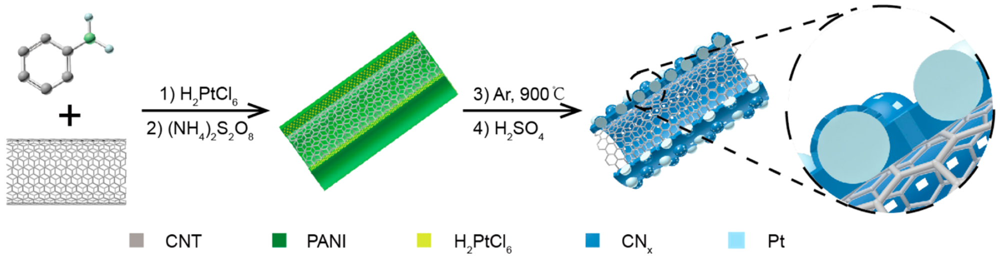

Figure 1. Schematic illustration of the preparation of Pt@CN*x*/CNT catalyst.

enhancement of catalyst performance and their application in practical PEMFCs. More importantly, the dissolution and migration of Pt have not been satisfactorily suppressed. Thus, new strategies to develop highly stable and efficient ORR catalysts are still extremely desirable but challenging.

Herein, we present a facile but effective strategy to embed Pt nanocrystals into N-doped porous carbon on carbon nanotubes (Pt@CN*x*/CNT). The embedding of Pt nanocrystals into a N-doped porous carbon layer not only effectively prevented the Pt nanocrystals from detachment, dissolution, migration, and aggregation during accelerated durability tests or heat-treatment at 900 °C, but also allowed access of the electrolyte to the Pt surface as a result of the porous structure and preserved good electron transfer from the CNTs by avoiding structural damage to the CNT surface, as compared with other strategies. The interaction between the embedded Pt nanocrystals and the encapsulating CN*x* shells was found in Pt@CN*x*/CNT, which would markedly affect the electronic structure of Pt nanocrystals and contribute to the improvement in catalytic activity and stability of the catalyst. As a result, the Pt@CN*x*/CNT catalyst exhibited excellent durability and sufficient catalytic activity for ORR.

2. EXPERIMENTAL SECTION

2.1. Synthesis of Pt@CN*x*/CNT Composite. Carbon nanotubes (CNT, Shenzhen Nanotech Port Co. Ltd.) were first ground for 10 h and then immersed in concentrated HCl solution for 5 days, followed by washing and vacuum drying at 80 °C overnight. A 100 mg portion of CNT and 100 mg of aniline monomer (distilled before use) were dispersed in 50 mL of HCl (1 M) aqueous solution and ultrasonicated for 1 h. Appropriate H_2PtCl_6 (38.5 mM) was then added into the dispersion. The mixture was stirred below 5 °C for 10 h to achieve a homogeneous dispersion, and then 50 mL of HCl (1 M) aqueous solution containing 245.2 mg of $(NH_4)_2S_2O_8$ (APS) was added dropwise under vigorous stirring (the molar ratio of APS to aniline was 1:1). The polymerization was conducted in an ice bath (<5 °C) for 20 h. After the polymerization, the liquid was evaporated at 50 °C under stirring. The obtained Pt-PANI/CNT product was washed with anhydrous alcohol and Milli-Q water and then dried under vacuum at 60 °C overnight. The sample was then pyrolyzed at 900 °C for 1 h under argon flow. Finally, the heat-treated sample was preleached in 1 M H_2SO_4 at 80 °C for 8 h and thoroughly washed in Milli-Q water. For comparison, the CN*x*/CNT was prepared in parallel under the above conditions but without the addition of H_2PtCl_6 solution.

2.2. Electrochemical Measurement. The cyclic voltammograms were carried out in a N_2-purged 0.1 M $HClO_4$ solution at a scan rate of 50 mV s^{-1}. The ORR polarization curves were recorded in O_2-saturated 0.1 M $HClO_4$ solution at a scan rate of 10 mV s^{-1} solution. The CV accelerating durability tests (ADT) were performed in N_2-purged 0.1 M $HClO_4$ by potential cycling between 0 and 1.2 V vs RHE at a scan rate of 50 mV s^{-1} at room temperature. The details for all electrochemical experiments and analysis are presented in the Supporting Information. The catalyst loadings of Pt@CN*x*/CNT and commercial Pt/C for all measurements were fixed to 22 μg_{Pt} cm^{-2}.

3. RESULTS AND DISCUSSION

The Pt@CN*x*/CNT catalyst was synthesized via a facile in situ reduction process, as illustrated in Figure 1. In brief, aniline monomer was first selectively adsorbed onto the CNT surface via $\pi-\pi$ interaction between the aniline and CNT. After the addition of the H_2PtCl_6 solution, the polymerization was initiated by the introduction of APS, which allowed the formation of a polyaniline layer on the CNTs and the encapsulation of Pt source inside the polyaniline layer. Afterward, the resulting product was sufficiently washed to remove $PtCl_6^{2-}$ species adsorbed on the outer surfaces of CNTs. The dried product was then heated at 900 °C for 1 h under flowing argon gas and then preleached in 1 M H_2SO_4 for 8 h to remove any unstable species in carbonized materials and expand the nanopores to make more Pt surface accessible to the electrolyte. During the pyrolysis process, the polyaniline layer was pyrolyzed into the N-doped porous carbon layer, and the Pt sources in the polyaniline layer were simultaneously reduced by carbon into the Pt nanocrystals, which were embedded in the resulting N-doped porous carbon layer. The typical overall Pt loading in Pt@CN*x*/CNT composite used in the following experiments was 13.01 wt %, determined by inductively coupled plasma atomic emission spectroscopy. It should be noted that the Pt loading in Pt@CN*x*/CNT can be easily tuned by adjusting the amount of Pt sources during the preparation of catalyst. Two examples with a Pt loading of 1.3 and 5.2 wt % were prepared. The TEM images shown in Figure S1 clearly demonstrate the distribution of Pt nanocrystals in the Pt@CN*x*/CNT was closely related to the Pt loading.

The crystalline structures of the prepared composite and the commercial Johnson Matthey (JM) Pt/C (20 wt %) catalyst for comparison were first analyzed by powder X-ray diffraction (XRD). Four major peaks at 39.76°, 46.26°, 67.55°, and 81.41° shown in both XRD patterns (Figure 2a) can be indexed well to the diffraction from (111), (200), (220), and (311) planes of cubic Pt (JCPDS 04-0802). The XRD peaks at 26.07°, 42.76°, and 53.66° in the composite can be attributed to diffraction from carbon nanotubes.[30,31] This result indicated that the product should be the composite of cubic Pt nanocrystals and carbon nanotubes. X-ray photoelectron spectroscopy (XPS) was further performed to determine the composition of the composite. The XPS spectrum (Figure S2) clearly exhibited the

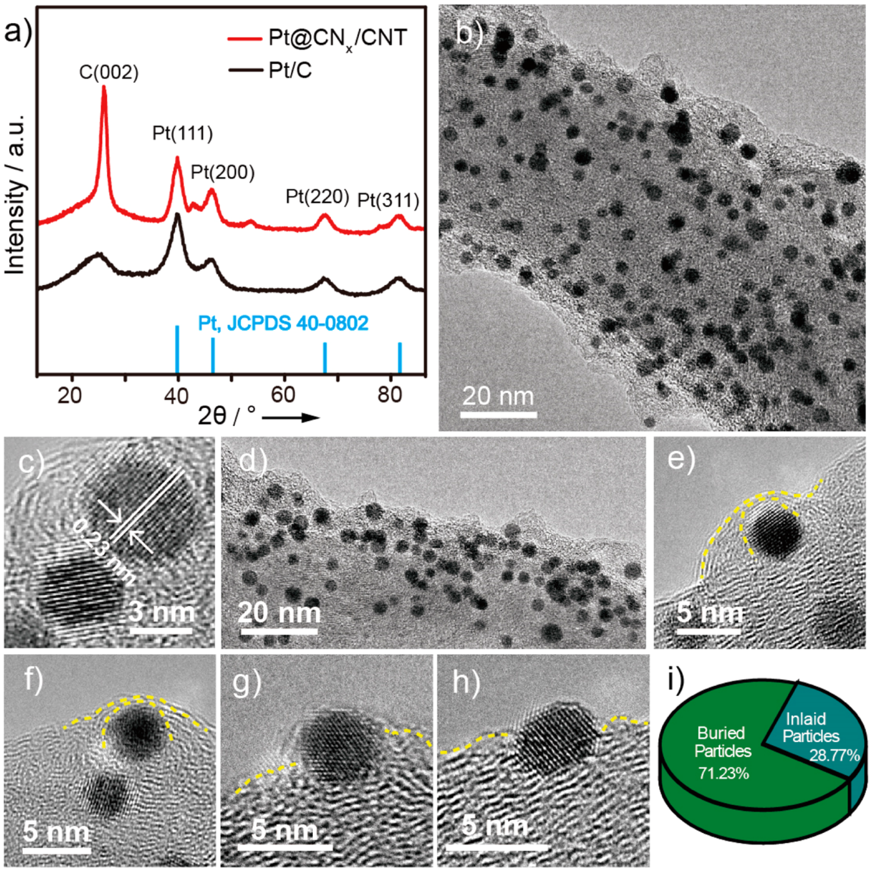

Figure 2. (a) XRD patterns of Pt@CN*x*/CNT and JM Pt/C; TEM images (b,d) and HRTEM images (c,e,f,g,h) of Pt@CN*x*/CNT; (i) The statistical pie diagram of Pt nanocrystals in different status in Pt@CN*x*/CNT catalyst.

signals of C 1s, N 1s, and Pt 4f, confirming the existence of element N and Pt in the product.

The morphologies and structure of the composite were investigated by transmission electron microscopy (TEM). The typical TEM image in Figure 2b displays the smooth surface of a CNT coated with a thin layer with a rough outer surface, which could be ascribed to a N-doped carbon layer (CN*x*) originating from the pyrolysis of polyaniline. Numerous nanoparticles in a narrow size distribution dispersed on the substrate without obvious aggregation can also be seen. The average particle size was 3.12 ± 0.87 nm, based on statistical analysis. The high-resolution TEM image (Figure 2c) shows clear and continuous lattice fringes throughout the particles, with a distance of 0.23 nm, which is consistent with the *d*-spacing of (111) planes of face-centered cubic (fcc) crystalline Pt, corroborating these nanoparticles are fcc Pt nanocrystals. Moreover, by closely looking at a large quantity of nanoparticles dispersed at the edge of a CNT during TEM observation, it was found that most of the Pt nanocrystals were buried in the CN*x* layer and coated with a few fractured carbon layers (Figure 2d−f), and some were inlaid in the CN*x* layer with partial surface exposed (Figure 2g,h). Almost no Pt nanoparticles directly attached on the outer surface like the ones in JM Pt/C were found.

A statistical analysis of over 200 Pt nanocrystals at the edge of CNT showed that 71.23% of the Pt nanocrystals were coated with carbon layers, and the rest were inlaid in the carbon (Figure 2i). It should be noted that these Pt nanocrystals were obtained and survived after the pyrolysis at 900 °C for 1 h. It is reasonable to believe that these nanocrystals (shown in Figure 2d−f and g,h) were buried or inlaid in the CN*x* layer because they would aggregate and grow into larger particles after such heat-treatment at 900 °C if they were just physically attached on the top of the CN*x* layer.

For comparison, the JM Pt/C catalyst, in which Pt nanoparticles are directly deposited on the carbon support with no encapsulating layer, was subjected to the same heat treatment and characterized. TEM images (Figure S3) manifests that Pt nanoparticles originally in ∼3 nm severely aggregated together and grew into larger particles in tens of nanometers after such a treatment. Therefore, it was reasonably believed that the CN*x* layer encapsulating the Pt nanocrystals effectively prevented them from immigration and aggregation. The CN*x* layer was also expected to keep Pt nanocrystals from peeling off or aggregating during the long-term electrochemical operation.

To evaluate the electrochemical performance of Pt@CN*x*/CNT and the effect of the CN*x* layer on catalytic performance for ORR, cyclic voltammograms (CV) and linear sweep voltammetry (LSV) experiments were first conducted on the Pt@CN*x*/CNT and JM Pt/C catalysts (20 wt % Pt) for comparison. The CV curves of both samples (Figure 3a) exhibit similar peaks associated with the adsorption/desorption of hydrogen and the formation/reduction of Pt oxides. The electrochemical surface area (ECSA) was calculated by measuring the Coulombic charge for hydrogen adsorption/desorption. The ECSA of Pt@CN*x*/CNT was estimated to be 74.29 $m^2\ g^{-1}$, 12.36% smaller than that of Pt/C (86.65 $m^2\ g^{-1}$). Considering the slightly larger size of the Pt nanocrystals in Pt@CN*x*/CNT (3.12 ± 0.87 vs 2.85 ± 0.60 nm) and the same

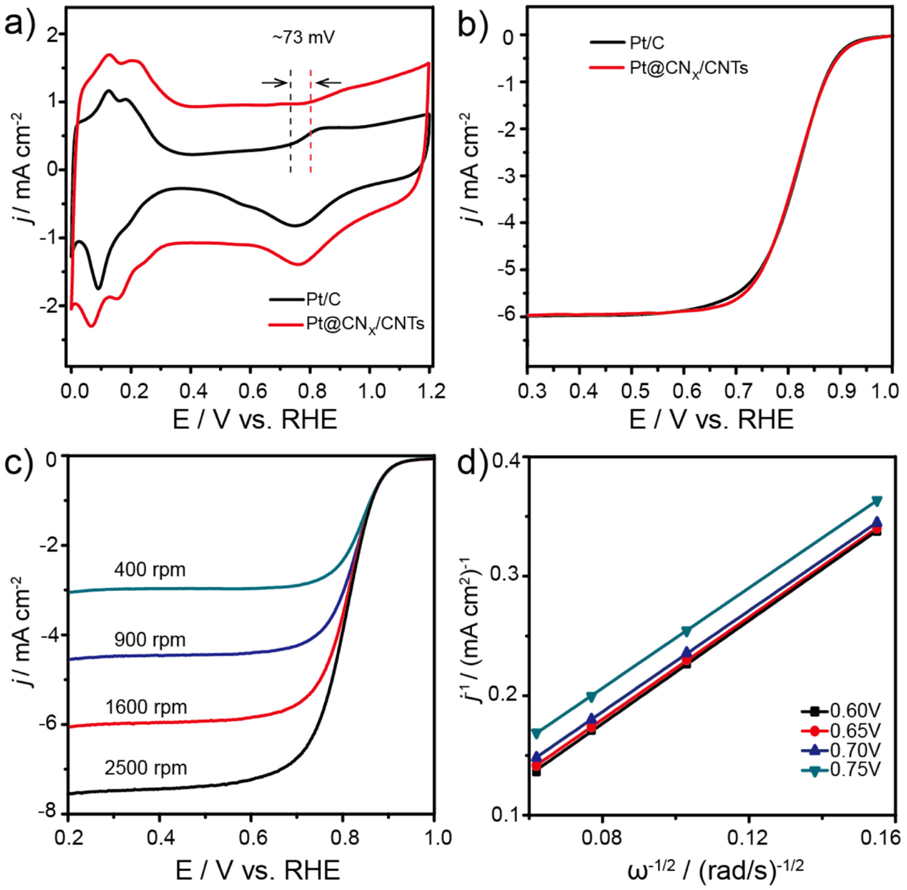

Figure 3. (a) CV curves of Pt@CN*x*/CNT and JM Pt/C recorded in N_2-purged 0.1 M $HClO_4$ solution at a scan rate of 50 mV s^{-1}; (b) ORR polarization curves of Pt@CN*x*/CNT and JM Pt/C recorded in O_2-saturated 0.1 M $HClO_4$ solution at room temperature (1600 rpm, sweep rate of 10 mV s^{-1}); (c) ORR polarization curves of Pt@CN*x*/CNT at different rotation speeds, recorded in O_2-saturated 0.1 M $HClO_4$ at room temperature, sweep rate 10 mV s^{-1}; (d) corresponding Koutecky−Levich plots at different potentials.

Pt loading on the electrodes, the decrease in ECSA for Pt@CN*x*/CNT could be reasonably attributed to the presence of the encapsulating CN*x* layer, which covered a part of the Pt active sites. Taking the nanospheres in 3.12 and 2.85 nm as models, the difference in surface area is about 8.66%. Therefore, a 12.36% loss in ECSA for Pt@CN*x*/CNT compared to Pt/C also implied that the CN*x* layer should have porous structures and allow access of the electrolyte to the surface of Pt nanocrystals. Comparing to the CV curves tested in N_2-saturated solution, CV curve of Pt@CN*x*-CNT recorded in O_2-saturated electrolyte (Figure S4) shows apparently enhanced cathodic current density and high sensitivity for ORR, indicating that oxygen can reach the surface of the Pt nanocrystals, and the porous structure should really exist in the Pt@CN*x*/CNT.

The N_2 adsorption−desorption experiment was further carried out to directly confirm the porous nature of the Pt@CN*x*/CNT. The Brunauer−Emmett−Teller (BET) analysis (Figure S5a) demonstrates that the Pt@CN*x*/CNT showed a high surface area of 308.8 m^2/g, which is much larger than that of pristine CNTs (79.5 m^2/g).[32] This value is comparable to the results reported by Kuo and Hsu.[33,34] The corresponding pore size distribution analysis (Figure S5b) clearly reveals the existence of a great quantity of nanopores. The diameter of most pores falls in a range of <1 nm or from 3 to 4 nm, which should be large enough for free diffusion of the oxygen molecule with a kinetic diameter of 0.346 nm.[35] As demonstrated by Karl et al.,[36] the Pt nanocrystals in the porous structure can be fully utilized in real fuel cells, and there are no limitations to the ionomer access through the porous structure. Therefore, the porous structure would not affect the transfer of oxygen and proton in real fuel cells. Furthermore, it should be noted that the onset potential of Pt oxidation in the Pt@CN*x*/CNT catalyst recorded in N_2-saturated solution was significantly shifted to more positive potential compared with that of JM Pt/C as indicated by vertical lines in Figure 3a, suggesting a delayed formation and weak adsorption of oxygenated species on Pt surfaces embedded in CN*x* layer and, thus, better durability during ORR.[22,27]

Moreover, the LSV measurements were carried out by using a rotating-disk electrode (RDE) operated at 1600 rpm in O_2-saturated 0.1 M $HClO_4$. Figure 3b shows typical ORR polarization curves recorded on RDEs coated with Pt@CN*x*/CNT and JM Pt/C as catalysts. It can be seen that Pt@CN*x*/CNT exhibited a very similar onset potential and half-wave potential compared with JM Pt/C, implying that the encapsulating CN*x* layer did not affect the catalytic activity of Pt@CN*x*/CNT for ORR. Considering the smaller ECSA of Pt@CN*x*/CNT vs JM Pt/C, the former demonstrated the higher specific activity. Although the CN*x*/CNT itself did not contribute much to the improved activity, as indicated by its very poor catalytic activity for ORR (Figure S6), the conductive network constructed by CN*x*/CNT, which enhanced the electron transfer in Pt@CN*x*/CNT during ORR, and the

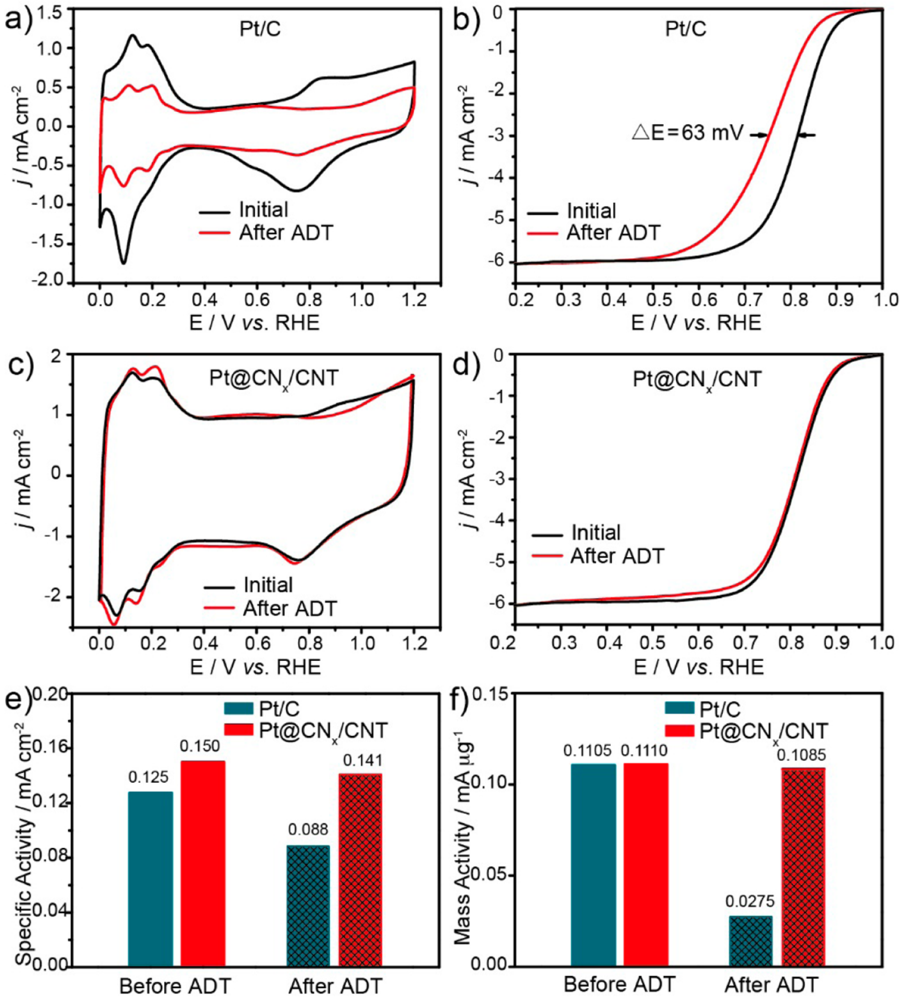

Figure 4. (a,c) CV curves, and (b,d) ORR polarization curves of JM Pt/C and Pt@CN*x*/CNT before (black) and after (red) ADT. (e,f) The comparison of (e) specific activities and (f) mass activities at 0.85 V vs RHE before and after ADT.

possible interaction between Pt nanocrystals and CN*x* layer (as discussed later on) should be responsible for the improvement of the catalytic activity.

To better understand the ORR kinetics of Pt@CN*x*/CNT, a set of polarization curves (Figure 3c) for ORR were recorded at varied rotation speeds in O_2-saturated 0.1 M $HClO_4$. The Koutecky−Levich plots calculated with these curves (Figure 3d) show good linearity and near parallelism of the fitting lines, indicating the first-order reaction kinetics toward the concentration of dissolved oxygen and similar electron transfer numbers for ORR at different potentials. The electron transfer number of Pt@CN*x*/CNT for catalyzing ORR was calculated to be ∼3.9 through the slopes of Koutecky−Levich plots, which is in good agreement with the theoretical value.

As mentioned above, the stability of an ORR catalyst is critical for the application of PEMFCs. To demonstrate the effectively stabilizing Pt nanocrystals by the CN*x* layer in the designed Pt@CN*x*/CNT catalysts, ADTs for Pt@CN*x*/CNT and JM Pt/C were thus carried out in N_2-purged 0.1 M $HClO_4$ solution by applying continuous potential sweeps between 0.0 and 1.2 V vs RHE for 1500 cycles at a scan rate of 50 mV s^{-1}. As indicated by CV curves and ORR polarization curves in Figure 4a,b, the JM Pt/C catalyst underwent ∼65% loss in ECSA after ADT (86.65 vs 30.91 m^2 g^{-1}), which was accompanied by an ∼60 mV negative shift of the half-wave potential in the ORR polarization curve; however, the Pt@CN*x*/CNT catalyst exhibited negligible changes in both ECSA (74.29 vs 75.46 m^2 g^{-1}, Figure 4c) and ORR activity (Figure 4d) after ADT. The small increase in ECSA of Pt@CN*x*/CNT could be ascribed to the slight corrosion of the CN*x* layer after ADT, which led to a slight increase in the exposed surface area of embedded Pt nanocrystals. This result could be corroborated by the small increase in the double layer capacitance, as shown in Figure 4c (red curve).

To directly compare the electrocatalytic activities of all evaluated catalysts for ORR, both the specific activity (Figure 4e) and the mass activity (Figure 4f) before and after ADT were calculated by using the Koutecky−Levich equation to represent the intrinsic activity of the catalysts. Pt@CN*x*/CNT delivered an ∼1.2 times larger area-specific activity, and a similar mass activity at the given potential compared with JM Pt/C before ADT. It was notably found that Pt@CN*x*/CNT exhibited negligible degradation in both the specific and mass activity after ADT (0.141 vs 0.150 mA cm^{-2} for specific activity, and 0.1085 vs 0.1110 mA μg^{-1} for mass activity). Compared to JM Pt/C, the specific and mass activity of Pt@CN*x*/CNT are ∼1.6 and ∼4 times larger after ADT, respectively.

The different degradation behaviors of JM Pt/C and Pt@CN*x*/CNT were further investigated by checking the morphologies of both catalysts before and after ADT with

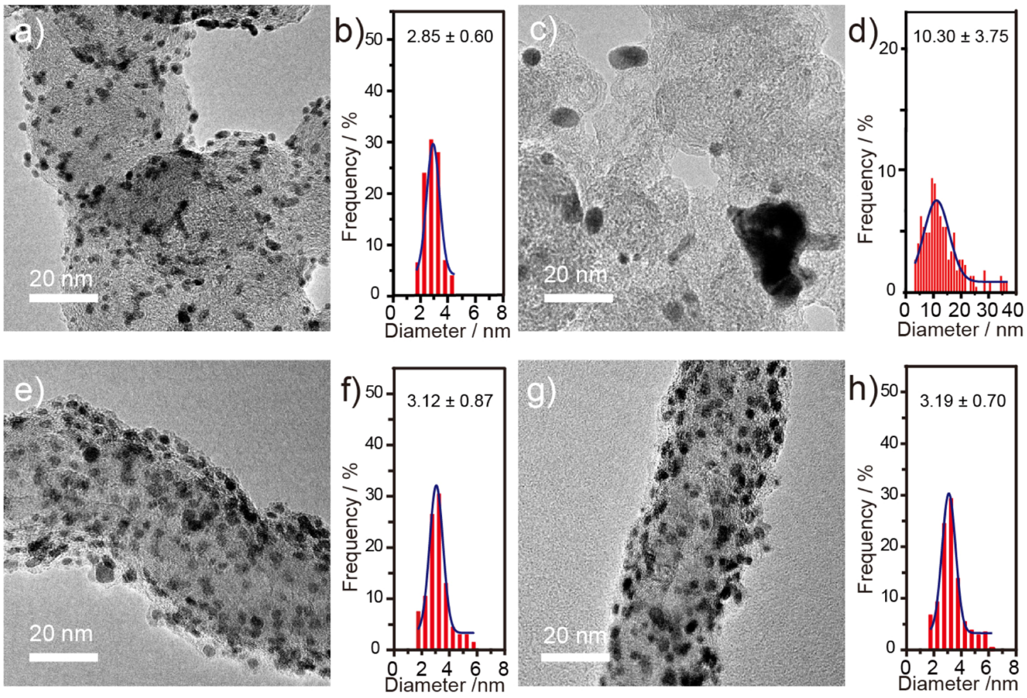

Figure 5. TEM images of JM Pt/C and the size distribution of Pt nanocrystals (a,b) before and (c,d) after ADT. TEM images of Pt@CN*x*/CNT and the size distribution of Pt nanocrystals (e,f) before and (g,h) after ADT.

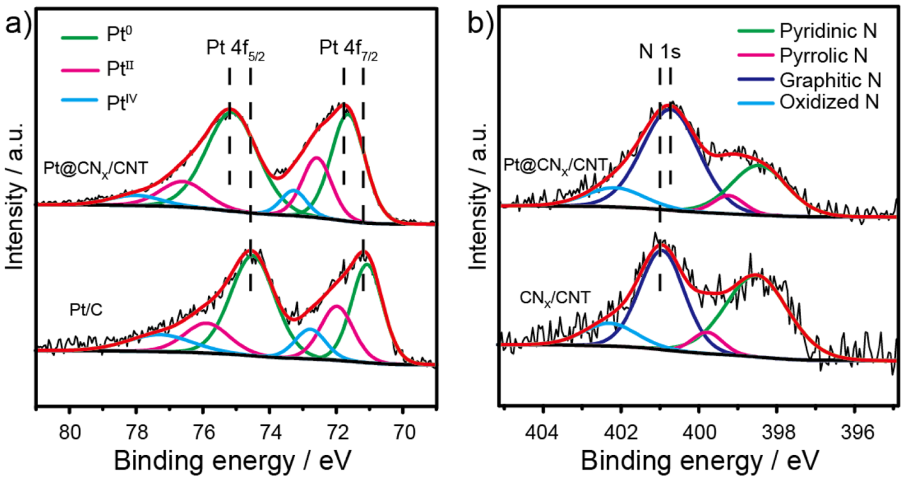

Figure 6. (a) XPS spectra showing the binding energy of Pt 4f in the Pt@CN*x*/CNT and JM Pt/C catalysts; (b) XPS spectra showing N 1s signals of Pt@CN*x*/CNT and CN*x*/CNT.

the TEM technique, as shown in Figure 5. The size distributions of Pt nanocrystals were also analyzed by randomly selecting over 200 Pt nanocrystals and measuring their diameters. Figure 5a−d demonstrates that Pt nanocrystals with an average diameter of 2.85 ± 0.60 nm were well-dispersed on the support in the JM Pt/C catalyst before ADT, but they aggregated and agglomerated severely into irregular larger nanoparticles with a size of 10.30 ± 3.75 nm after ADT. This was consistent with a dramatic decrease in the ECSA (65% loss). In contrast, the morphology of Pt@CN*x*/CNT did not appreciably change before and after ADT (Figure 5e−h). No obvious aggregation or peel-off of Pt nanocrystals were observed in TEM observation, indicating that the encapsulating CN*x* layer accommodated these nanocrystals very well and prevented them from dissolving, migrating, aggregating, and growing. This result accounted for the excellent stability of Pt@CN*x*/CNT in catalyzing ORR.

Furthermore, to investigate the possible interaction between Pt nanocrystals and the support, high-resolution XPS signals of Pt 4f and N 1s were deconvoluted into the corresponding components, as presented in Figure 6. By comparing the XPS peaks of Pt@CN*x*/CNT and JM Pt/C, it could be seen that the binding energies for both Pt 4f5/2 and 4f7/2 peaks in Pt@CN*x*/CNT shifted positively by ~0.76 eV relative to JM Pt/C (Figure 6a). This shift in binding energy could be ascribed to the electronic interaction between the embedded Pt nanocrystals and the encapsulating CN*x* layer, which was corroborated by the shift of the N 1s peak in Pt@CN*x*/CNT toward a lower binding energy compared with that in pure CN*x*/CNT (Figure 6b). It was believed that the electronic interaction between the Pt nanocrystals and CN*x* layer would affect the electronic structures of the surface atoms in the Pt nanocrystals and, thus, the adsorption/desorption of oxygen species on their surface, which would contribute to the improvement of the stability and catalytic activity in Pt@CN*x*/CNT. This result was consistent with a positive shift in the onset potential associated with Pt oxidation in Pt@CN*x*/CNT catalyst (Figure 3a).

4. CONCLUSIONS

In summary, to address the issue of durability in supported noble-metal-based electrocatalysts, an effective strategy was developed to embed Pt nanocrystals into porous carbon shells on a carbon nanotube substrate by means of precursor polymerization, pyrolysis, and in situ reduction. The fixation of Pt nanocrystals inside a porous CN*x* layer not only restrained the Pt nanocrystals from detachment, dissolution, migration, and aggregation during accelerated durability tests or heat-treatment at 900 °C, but also maintained their catalytic activity. A benefit from this unique structure as well as the electronic interaction between the embedded Pt nanocrystals and the encapsulating CN*x* layer, the developed Pt@CN*x*/CNT electrocatalysts exhibited an excellent durability and efficient catalytic activity for ORR. The demonstrated strategy could be easily extended to produce a wide range of other electrocatalysts with extraordinary stability.

■ ASSOCIATED CONTENT

Ⓢ Supporting Information

The following file is available free of charge on the ACS Publications website at DOI: 10.1021/acscatal.5b00117.

> Experimental details, TEM images with different Pt loadings, XPS spectrum, TEM images of JM Pt/C before and after heat treatment, CV curves in O_2-saturated 0.1 M $HClO_4$, N_2 adsorption−desorption isotherm and pore size distribution, ORR polarization curve of CN_x/CNT (PDF)

■ AUTHOR INFORMATION

Corresponding Authors

*E-mail: hujs@iccas.ac.cn.
*E-mail: zdwei@cqu.edu.cn.

Notes

The authors declare no competing financial interest.

■ ACKNOWLEDGMENTS

We acknowledge financial support from the National Key Project on Basic Research (2015CB932302, 2012CB215500, and 2011CB808701), the National Natural Science Foundation of China (91127044 and 21173237), and the Strategic Priority Research Program of the Chinese Academy of Sciences (Grant No. XDB12020100).

■ REFERENCES

(1) Gasteiger, H. A.; Marković, N. M. *Science* **2009**, *324*, 48−49.

(2) Zhou, X.; Qiao, J.; Yang, L.; Zhang, J. *Adv. Energy Mater.* **2014**, *4*, 1301523.

(3) Ferreira, P. J.; la O', G. J.; Shao-Horn, Y.; Morgan, D.; Makharia, R.; Kocha, S.; Gasteiger, H. A. *J. Electrochem. Soc.* **2005**, *152*, A2256−A2271.

(4) Mayrhofer, K. J. J.; Meier, J. C.; Ashton, S. J.; Wiberg, G. K. H.; Kraus, F.; Hanzlikb, M.; Arenz, M. *Electrochem. Commun.* **2008**, *10*, 1144−1147.

(5) Wang, Y. J.; Wilkinson, D. P.; Zhang, J. J. *Chem. Rev.* **2011**, *111*, 7625−7651.

(6) Shao, Y. Y.; Yin, G. P.; Gao, Y. Z. *J. Power Sources* **2007**, *171*, 558−566.

(7) Gasteiger, H. A.; Kocha, S.; Sompalli, B.; Wagner, F. T. *Appl. Catal., B* **2005**, *56*, 9−35.

(8) Tang, H.; Qi, Z.; Ramani, M.; Elter, J. F. *J. Power Sources* **2006**, *158*, 1306−1312.

(9) Zhang, S.; Yuan, X. Z.; Hin, J. N. C.; Wang, H.; Friedrich, K. A.; Schulze, M. *J. Power Sources* **2009**, *194*, 588−600.

(10) Perez-Alonso, F. J.; Elkjær, C. F.; Shim, S. S.; Abrams, B. L.; Stephens, I. E. L.; Chorkendorff, I. *J. Power Sources* **2011**, *196*, 6085−6091.

(11) Meier, J. C.; Galeano, C.; Katsounaros, I.; Topalov, A. A.; Kostka, A.; Schüth, F.; Mayrhofer, K. J. J. *ACS Catal.* **2012**, *2*, 832−843.

(12) Chen, S.; Wei, Z.; Qi, X.; Dong, L.; Guo, Y.; Wan, L.; Shao, Z.; Li, L. *J. Am. Chem. Soc.* **2012**, *134*, 13252−13255.

(13) Guo, L.; Chen, S.; Wei, Z. *J. Power Sources* **2014**, *255*, 387−393.

(14) Kou, R.; Shao, Y.; Mei, D.; Nie, Z.; Wang, D.; Wang, C.; Viswanathan, V. V.; Park, S.; Aksay, I. A.; Lin, Y.; Wang, Y.; Liu, J. *J. Am. Chem. Soc.* **2011**, *133*, 2541−2547.

(15) Kibsgaard, J.; Gorlin, Y.; Chen, Z.; Jaramillo, T. F. *J. Am. Chem. Soc.* **2012**, *134*, 7758−7765.

(16) Liang, H. W.; Cao, X.; Zhou, F.; Cui, C. H.; Zhang, W. J.; Yu, S. H. *Adv. Mater.* **2011**, *23*, 1467−1471.

(17) Xia, B. Y.; Wu, H. B.; Yan, Y.; Lou, X. W.; Wang, X. *J. Am. Chem. Soc.* **2013**, *135*, 9480−9485.

(18) Sun, S.; Zhang, G.; Geng, D.; Chen, Y.; Li, R.; Cai, M.; Sun, X. *Angew. Chem.* **2011**, *123*, 442−446.

(19) Shui, J. L.; Chen, C.; Li, J. C. M. *Adv. Funct. Mater.* **2011**, *21*, 3357−3362.

(20) Chen, Z.; Waje, M.; Li, W.; Yan, Y. *Angew. Chem., Int. Ed.* **2007**, *46*, 4060−4063.

(21) Yoo, S. J.; Kim, S. K.; Jeon, T. Y.; Hwang, S. J.; Lee, J. G.; Lee, S. C.; Lee, K. S.; Cho, Y. H.; Sung, Y. E.; Lim, T. H. *Chem. Commun.* **2011**, *47*, 11414−11416.

(22) Wang, R.; Xu, C.; Bi, X.; Ding, Y. *Energy Environ. Sci.* **2012**, *5*, 5281−5286.

(23) Vinayan, B. P.; Nagar, R.; Rajalakshmi, N.; Ramaprabhu, S. *Adv. Funct. Mater.* **2012**, *22*, 3519−3526.

(24) Escudero-Escribano, M.; Verdaguer-Casadevall, A.; Malacrida, P.; Grønbjerg, U.; Knudsen, B. P.; Jepsen, A. K.; Rossmeisl, J.; Stephens, I. E. L.; Chorkendorff, I. *J. Am. Chem. Soc.* **2012**, *134*, 16476−16479.

(25) Kumar, A.; Ramani, V. *ACS Catal.* **2014**, *4*, 1516−1525.

(26) Huang, S. Y.; Ganesan, P.; Park, S.; Popov, B. N. *J. Am. Chem. Soc.* **2009**, *131*, 13898−13899.

(27) Chen, S.; Wei, Z.; Guo, L.; Ding, W.; Dong, L.; Shen, P.; Qi, X.; Li, L. *Chem. Commun.* **2011**, *47*, 10984−10986.

(28) Ho, V. T. T.; Pan, C. J.; Rick, J.; Su, W. N.; B. Hwang, J. *J. Am. Chem. Soc.* **2011**, *133*, 11716−11724.

(29) Ma, X. M.; Meng, H.; Cai, M.; Shen, P. K. *J. Am. Chem. Soc.* **2012**, *134*, 1954−1957.

(30) Yu, H.; Zeng, K.; Fu, X.; Zhang, Y.; Peng, F.; Wang, H.; Yang, J. *J. Phys. Chem. C* **2008**, *112*, 11875−11880.

(31) Logeswari, J.; Pandurangan, A.; Sangeetha, D. *Ind. Eng. Chem. Res.* **2011**, *50*, 13347−13354.

(32) Jiang, W.-J.; Hu, J.-S.; Zhang, X.; Jiang, Y.; Yu, B.-B.; Wei, Z.-D.; Wan, L.-J. *J. Mater. Chem. A* **2014**, *2*, 10154−10160.

(33) Kuo, P. L.; Hsu, C. H. *ACS Appl. Mater. Interfaces* **2011**, *3*, 115−118.

(34) Hsu, C. H.; Kuo, P. L. *J. Power Sources* **2012**, *198*, 83−89.

(35) Breck, D. W. *Zeolite Molecular Sieves; Structure, Chemistry and Use*; John Wiley and Sons: New York, 1973; p 636.

(36) Galeano, C.; Meier, J. C.; Peinecke, V.; Bongard, H.; Katsounaros, I.; Topalov, A. A.; Lu, A.; Mayrhofer, K. J. J.; Schüth, F. *J. Am. Chem. Soc.* **2012**, *134*, 20457−20465.